AAS 22-545

ORBIT MAINTENANCE BURN DETAILS FOR SPACECRAFT IN A NEAR RECTILIENAR HALO ORBIT

Diane C. Davis,[*] Stephen T. Scheuerle,[†] Dale A. Williams,[‡] Frederick S. Miguel,[§] Emily M. Zimovan-Spreen,[**] and Kathleen C. Howell[††]

The baseline orbit for Gateway is a Near Rectilinear Halo Orbit (NRHO) in a 9:2 resonance with the lunar synodic period. A spacecraft in this slightly unstable NRHO requires orbit maintenance (OM) for long-duration operations. An updated OM algorithm is described, including a discussion of desirable OM burn locations along the NRHO and the effects of changing weighting parameters and tolerances. The directions of the OM burns are explored in depth, both in the Earth-Moon rotating frame and from a Sun-relative perspective. A technique to augment the OM algorithm to enable long-term operations in NRHO is outlined, and the effects of constraints on OM attitudes are investigated.

INTRODUCTION

Near Rectilinear Halo Orbits (NRHOs)[1] are of recent focus across NASA and the space industry. Members of the halo orbit families originating around both L1 and L2, Earth-Moon NRHOs exhibit marginally stable, or nearly stable, behavior in the vicinity of the Moon. Two upcoming spacecraft, CAPSTONE and Gateway, are planned to fly in a southern L2 NRHO near the Moon. The Gateway is proposed as a crew-tended outpost in cislunar space: a proving ground for deep space technologies and a staging location for missions to the lunar surface and beyond Earth orbit. The first components of Gateway are planned to launch in 2024. CAPSTONE is a cubesat launched in 2022 that will serve as a pathfinder mission for Gateway and a demonstration of navigation technologies. Both spacecraft share a similar baseline orbit: an NRHO in a 9:2 resonance with the lunar synodic period, completing 9 revolutions around the Moon every 2 lunar synodic months, and phased to avoid long eclipses from the Earth's shadow. This 9:2 NRHO is slightly unstable, and an unmaintained spacecraft inserted into the NRHO departs within several months as a result of inherent instability as well as perturbations and errors associated with operational spacecraft. For a spacecraft to remain in the NRHO for a reasonable lifetime, a low-cost, reliable orbit maintenance (OM) algorithm is required.

Previous studies outline an OM strategy employing an x-axis crossing control algorithm,[2,3,4] and later analyses augment the originally proposed method to maintain an eclipse-favorable phase within the selected NRHO.[5,6,7] The current investigation outlines the latest evolution of the orbit maintenance algorithm planned for the Gateway in NRHO. Using Gateway as a simulation spacecraft, this analysis explores the cost of OM over time and the divergence of the trajectory from the baseline NRHO. The OM burns are influenced by the dynamics of the NRHO. The investigation explores OM burn direction with respect to the Earth-Moon and Sun-spacecraft reference frames. The selected reference frames offer insight into the governing flow in the

[*] Principal Systems Engineer, a.i. solutions, Inc.
[†] Ph.D. Student, School of Aeronautics and Astronautics, Purdue University
[‡] Graduate Student, School of Aeronautics and Astronautics, Purdue University.
[§] Senior Systems Engineer, a.i. solutions, Inc.
[**] Aerospace Engineer, Flight Mechanics and Trajectory Design Branch, NASA Johnson Space Center.
[††] Hsu Lo Distinguished Professor, School of Aeronautics and Astronautics, Purdue University.

vicinity of the orbit as well as attitude limitations in mission operation. The robustness or the OM is considered in the presence of attitude constraints, and long-term behavior is explored.

BACKGROUND AND DYNAMICAL MODELS

The NRHO selected as the Gateway's baseline exhibits a 9:2 resonance with the lunar synodic period, completing 9 revolutions around the Moon every 2 lunar synodic months. The phase within the NRHO is designed to avoid passing through the Earth's shadow.[8] With an orbital period of approximately 6.5 days, the orbit is bounded by an apolune radius of about 71,000 km and a perilune radius of about 3,500 km. The NRHO is characterized by a stability index[9] of approximately 1.3, where a stability index of 1 signifies a marginally stable orbit in a linearized model. With a stability index larger than unity, the 9:2 NRHO is inherently unstable; however, the low value of stability index implies that natural departure from the NRHO occurs slowly. Orbit maintenance costs in this orbit are low, and the NRHO is robust to missed, delayed, or waived maneuvers for several revolutions. The southern 9:2 L2 NRHO appears in Figure 1 in Earth-Moon and Sun-Earth rotating views.

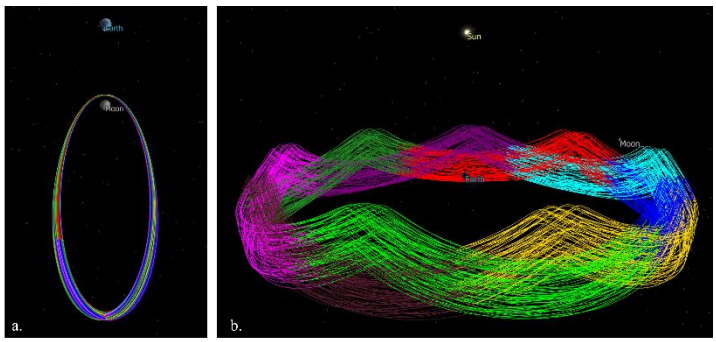

Figure 1. 15-year Gateway baseline NRHO in Earth-Moon (a) and Sun-Earth (b) rotating views.

The analysis summarized here is primarily performed using two software packages and two dynamical models. Circular Restricted 3-Body Problem (CR3BP) analysis is performed in Matlab, and analysis in a higher-fidelity ephemeris model is performed in the FreeFlyer astrodynamics software package. The CR3BP describes the motion of a massless spacecraft affected by two primary gravitational bodies such as the Earth and the Moon. The model assumes that the two primary bodies are point masses orbiting their center of mass in circular orbits. The spacecraft moves freely under the influence of the two primaries, and its motion is described relative to a reference frame that rotates along with the primaries. No closed-form solution exists to the CR3BP equations of motion, but five equilibrium solutions, the libration points, are denoted L1 through L5. Stable and unstable periodic orbit families, including the L2 halo orbits, emerge in the vicinity of the libration points. The CR3BP is an autonomous system, and without epoch dependence, the CR3BP provides a framework for understanding the characteristics of behavior in the cislunar regime that persist in higher-fidelity models. The higher-fidelity ephemeris model employed in the current investigation incorporates N-body equations of motion and NAIF planetary ephemerides. Integration is performed in a Moon-centered J2000 inertial coordinate frame with point-mass perturbations by the Sun and Earth included. The Moon's gravity is modeled using the GRAIL (GRGM660PRIM) model truncated to degree and order 8. Solar radiation pressure (SRP) acting on a sphere is also included in the force modeling of the simulated spacecraft.

For Monte Carlo analyses applying the OM algorithm, a baseline set of errors is defined. The baseline errors outlined here are modified as noted to assess their impact on the solutions. Each OM maneuver is associated with a zero-mean navigation error on the spacecraft state; 3σ position errors of 1.5 km and velocity errors of 0.8 cm/s are assumed. Maneuver execution errors are applied in a random direction to each OM burn with 3σ values of 1.5% in magnitude and 1° in direction with an additional fixed component of 1.42 mm/s (3σ). Mismodeling in SRP assumptions are assumed at 15% error in area and 30% error in coefficient of reflectivity (3σ); the spacecraft is assumed to have an area to mass ratio of 0.02 m^2/kg. Momentum wheel desaturations are assumed to occur 4 times per revolution: once near apolune prior to OM burns, and the rest centered around perilune, where the spacecraft experiences gravity gradient torques. A translational Δv with a 3σ value of 1 cm/s is applied in a random direction to simulate each desaturation. Perturbations are implemented as Gaussian errors with zero mean. The errors are summarized in Table 1.

Table 1. Baseline error models

	Error Type	3σ value	notes
SRP errors	Srp area Error %	30	a/m = 0.01
	Srp CR Error %	15	
Desaturation error	Random Δv (cm/s)	1	3 at perilune, 1 prior to OM burn
Navigation errors	Position error (km)	1.5	at each OM burn
	Velocity error (cm/s)	0.8	
Maneuver execution errors	percent magnitude %	1.5	at each OM burn
	fixed magnitude (mm/s)	1.42	
	direction (deg)	1	

GATEWAY ORBIT MAINTENANCE ALGORITHM

The simple OM algorithm designed for the Gateway NRHO employs an *x*-axis crossing control strategy adapted from previous halo orbit missions such as ARTEMIS[10] and WIND[11] to maintain both the NRHO characteristics as well as the eclipse-favorable phase within the NRHO. Originally outlined in a previous investigation,[5] the OM algorithm is updated in the current investigation to accommodate operational considerations such as realistic orbit determination (OD) data cutoff constraints. The algorithm makes use of a long-horizon baseline orbit that serves as a catalog of target states in the targeting process. A maneuver adjusts the spacecraft trajectory to target component(s) of the baseline orbit along a receding horizon. The placement of the maneuver and target, the components targeted, and the length of the targeting horizon all affect the cost and robustness of the orbit maintenance algorithm. The target is placed at the *x*-*z* plane crossing near perilune, or at the nearby perilune itself, as this target location is observed to lead to lower orbit maintenance costs. The maneuver, on the other hand, is placed away from perilune to avoid introducing errors at the sensitive region near the Moon, which can lead to algorithm divergence. A targeting horizon of approximately 6.2 revolutions balances cost with reliability. That is, the algorithm executes a maneuver to target the selected parameters from the baseline NRHO at perilune 6.2 revolutions downstream.

A single component of the baseline trajectory is one option as a target: the *x*-component of rotating velocity in the Earth-Moon rotating frame, v_x. Targeting the single component results in a trajectory that remains near the baseline for low cost but does not maintain the eclipse-favorable phase. After a 2-year simulation, for example, the perilune passage time drifts relative to the baseline by as much as 20 hours. At the end of 15 years, the perilune passage time can drift by as much as 600 hours relative to the baseline. With sufficient drift, the spacecraft is at risk of long eclipses by the Earth's shadow. Additionally, a varying phase complicates mission planning for visiting vehicles. Finally, as the Gateway trajectory drifts away from the baseline in phase, the OM targets become increasingly inaccurate representations of ballistic behavior, and OM costs increase.

To address these challenges, a second target is added to maintain the phase of the spacecraft within the NRHO; that is, to ensure the time of perilune passage remains near the baseline values throughout the spacecraft lifetime. In the updated OM algorithm, maneuvers are placed along each revolution at a specified value of osculating true anomaly, for example TA = 200º, or approximately one day prior to perilune passage. A differential corrector is employed to initially design a maneuver that delivers a downstream velocity that is targeted to meet the constraint at a subsequent perilune passage, i.e.,

$$v_x = v_{xref} \pm v_{tol} \tag{1}$$

where v_x is the *x*-component of the rotating velocity at the controlled spacecraft's perilune passage in the Earth-Moon rotating frame at the target horizon downstream, v_{xref} is the *x*-component of rotating velocity along the baseline NRHO at its respective perilune passage, and v_{xtol} is the targeting tolerance. The targeting horizon is initially set to 6.2 revolutions, so that the Eq (1) is satisfied at the seventh perilune passage downstream from the maneuver. If the targeter fails to converge, the targeting horizon is reduced successively until convergence is achieved. The resulting Δv is used as an initial guess to subsequently target both v_x and a weighted perilune passage time. The weighting is implemented by defining a target epoch

$$t_{targ} = W_t\left(t_{pref} - t_p\right) + t_p \tag{2}$$

where W_t is an empirically selected weighting factor, t_{pref} is the perilune passage time along the baseline NRHO, and t_p is the perilune passage time achieved by the maintained spacecraft after each iteration. The targeter is then executed such that

$$t_p = t_{targ} \pm t_{tol} \tag{3}$$

where t_{tol} is the targeting tolerance. The algorithm is then summarized as follows:

- Step spacecraft to the burn location, for example, TA = 200°
- Target $v_x = v_{xref} \pm v_{tol}$ at perilune 6.2 revolutions downstream (Eq. 1)
- If convergence fails, reduce targeting horizon to an earlier perilune passage until convergence is achieved
- Do not execute maneuver. Use computed Δv as an initial guess to target:
    - $v_x = v_{xref} \pm v_{tol}$ (Eq. 1) **and**
    - $t_p = t_{targ} \pm t_{tol}$ at perilune 6.2 revolutions downstream (Eq. 2)
- If convergence fails, reduce targeting horizon until convergence is achieved
- If $|\Delta v| > \Delta v_{min}$, execute maneuver. Otherwise waive maneuver.

With appropriate values selected for the burn location, the tolerances v_{tol} and t_{tol}, the weighting parameter W_t, and the minimum maneuver threshold Δv_{min}, this algorithm effectively maintains a spacecraft along the baseline NRHO over long durations in the presence of reasonable operational errors. A set of nominal parameters appears in Table 2. Sample results from the algorithm appear in Figure 2 for 100 Monte Carlo trials, each representing 112 revolutions, or approximately 2 years of uncrewed operations in the NRHO, and with errors applied as summarized in Table 1. The cumulative Δv for each trial appears in Figure 2a. The mean annual Δv across the 2-year simulation is 1.25 m/s; the maximum and minimum values are 1.0 m/s and 1.7 m/s respectively. The individual OM maneuvers (OMMs) appear in Figure 2b. The majority of the OMMs remain below 10 cm/s in magnitude, with occasional costs exceeding 15 cm/s. Many of the targeted OMMs do not meet the minimum maneuver threshold of 3 cm/s and are not executed; the mean number of burns waived per trial is 69 out of 110 opportunities; that is, in this example, nearly 63% of revolutions within the NRHO do not require an executed OMM in this simulation of a quiet, uncrewed spacecraft. As the spacecraft orbits in the NRHO, its state varies somewhat from the baseline since only two components (v_x and t_p) are targeted. The delta t_p relative to the baseline, measured at each perilune passage, appears in Figure 2c. With algorithm parameters set as defined in Table 2, t_p remains within 0.8 hours of baseline value throughout the 3-year simulation. Similarly, the deltas in the rotating x, y, and z position components of the state vector relative to the baseline, measured in the Earth-Moon rotating frame at each perilune passage, appear in Figure 2d. The deltas in the state are dominated by the z component but generally remain within 60 km of the baseline values.

Table 2. Nominal OM algorithm parameters

OMM TA	v_{tol}	t_{tol}	W_t	Δv_{min}	Horizon
200º	0.45 m/s	15 min	0.3	3 cm/s	6.2 revs

The full results of the Monte Carlo simulation summarized in Figure 2 offer insight into the broad landscape, but it is also illuminating to look more closely at individual trials. Three sample trials appear in Figure 3 for 18 revolutions each. The horizontal axis represents the revolution along the NRHO, and the vertical axis represents the targeted Δv magnitude of the OM burn each revolution, whether or not the burn is executed. The blue dashed line represents Δv_{min}. Any OMM with a targeted magnitude under this threshold is waived, while each OM burn with a magnitude greater than the threshold is executed. For each of the three trials, shown by blue, red, and aqua curves, the first three OMM magnitudes fall below the threshold and are not executed. Note the typical behavior prior to the execution of an OMM (denoted here as "antecedent growth rate"): each revolution, the targeted OMM magnitude grows as the errors in the trajectory increase. The magnitude continues to increase along with the trajectory errors until it exceeds the minimum maneuver threshold, set to 3 cm/s. A typical antecedent growth is highlighted in blue during the first 6 revolutions of the simulation. Once Δv_{min} is exceeded, as at revolution 6 along the blue curve, an OMM is executed, and the errors built up in the trajectory are reduced. Likewise, the subsequent targeted ΔV magnitude is reduced in a typical case since the trajectory errors have been corrected.

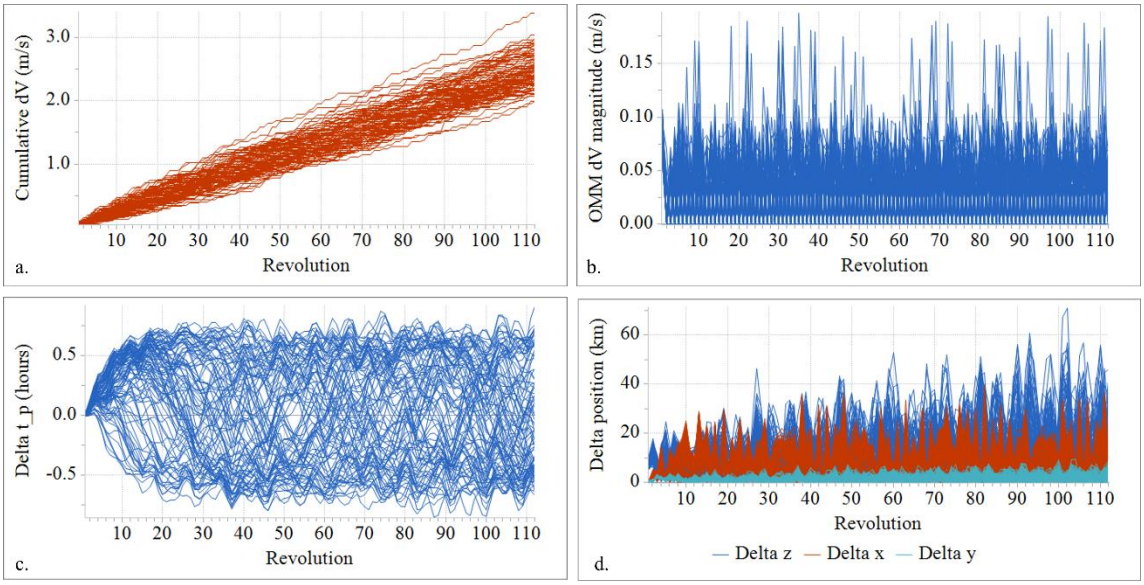

Figure 2. Two-year, 100-trial Monte Carlo simulation results for an uncrewed, quiescent spacecraft.

Other patterns are also apparent in Figure 3. A "staggered recovery" occurs when a steeper error growth is experienced. A sample staggered recovery appears in the red trial. In this case, the OMM at revolution 6 reduces the trajectory error sufficiently so that the OM burn at revolution 7 is just under the threshold; then, the OM burn at revolution 8 is relatively large, and for the next 6 revolutions, alternating OMMs exceed the threshold. Also apparent in the red curve is growth in the OM burn magnitude at revolution 18, even though the burn at revolution 17 is executed. Conversely, a slow antecedent growth rate is observed in the blue trajectory after the OM burn at revolution 10 very effectively reduces the trajectory error. The aqua curve exhibits typical behavior throughout the 18 revolutions.

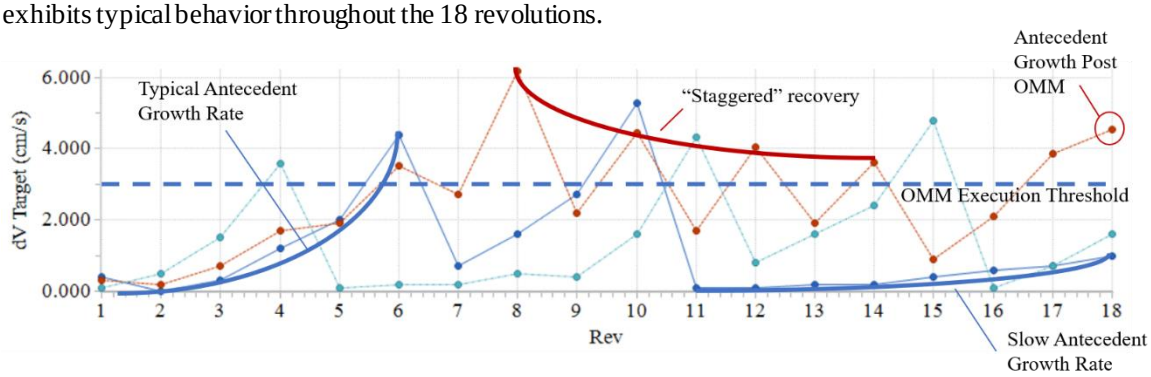

Figure 3. OM Δv targets for three sample Monte Carlo trials over 18 revolutions.

ORBIT MAINTENANCE MANEUVER DIRECTIONS

The OM burns serve to correct statistical errors built up over time in the NRHO. Unlike reboost maneuvers for a spacecraft in low Earth orbit, the NRHO OMMs do not primarily correct for predictable accelerations like atmospheric drag. Instead, the direction of each OM burn is not known until the revolution containing the OM burn execution. However, patterns governed by the dynamics of the NRHO do exist in the OMM directions.

The goal of an OMM is to restore a diverging trajectory closer to the baseline path. An outline of the procedure offers insight into the corrections process, and by extension, the resulting burn directions. At the initial time, the spacecraft is at some location in the vicinity of the baseline orbit. The ideal location for the spacecraft is to be precisely on the baseline; however, due to inevitable navigation and spacecraft errors, the

spacecraft is not exactly following the reference trajectory. Consider the initial error off the reference as $\delta\bar{x}_e$. The components of the vector column vector $\delta\bar{x}_e$ are written as,

$$\delta\bar{x}_e = [\delta x_e \quad \delta y_e \quad \delta z_e \quad \delta\dot{x}_e \quad \delta\dot{y}_e \quad \delta\dot{z}_e]' \tag{4}$$

In addition to the error in state, the process accounts for the error in timing or phase. The variation in time is denoted as δt_e and describes the difference in timing along the path between the baseline orbit and the current trajectory. Computing the error values for both state and timing is nontrivial, as there is a dependency on the phase. The errors in state and time are determined by propagating the spacecraft forward to the target perilune and comparing the spacecraft to the baseline. For an OMM placed at TA = 200°, the target perilune occurs roughly 6.2 revolutions ahead in the orbit (40.5 days). The error in time is determined by taking the difference between the corresponding perilune epoch of the reference and the propagated spacecraft, while the state error vector, $(\delta\bar{x}_{e,f})$ is computed by taking the difference between the reference state and the propagated spacecraft. After the errors are determined, a maneuver is applied at the initial time to help mitigate divergence from the baseline. The OMM is written as the column vector $\delta\bar{x}_{OMM}$. As the maneuver is only applied in the velocity components, the vector is written,

$$\delta\bar{x}_{OMM} = [0 \quad 0 \quad 0 \quad \dot{x}_{OMM} \quad \dot{y}_{OMM} \quad \dot{z}_{OMM}]' \tag{5}$$

Determining the direction and magnitude of the maneuver depends on the formulation of the differential corrections strategy. In the current investigation, a linear Newton-Raphson method is devised to target a downstream state on the reference trajectory. The state transition matrix (STM), a linear approximation of the dynamics, is applied to map an initial perturbation from the flow to a final deviation, and, thus, provides insight into the resulting OMM directions. The STM satisfies,

$$\delta\bar{x}_f = \Phi(t_f, t_0)\delta\bar{x}_i \tag{6}$$

where δx_f is the final deviation from a trajectory, δx_i is the initial perturbation, $\Phi(t_f, t_0)$ is the STM, and the terms t_0 and t_f refer to the initial and final times, respectively. The STM is dependent on the initial state; therefore, selecting a new location to perform an OMM alters the predicted maneuver directions. For this scenario, the STM is computed based on the reference trajectory, and the spacecraft follows a perturbed path from the baseline. The map of the STM is written as,

$$\Phi(t_f, t_0) = \begin{bmatrix} \frac{\delta x_f}{\delta x_0} & \cdots & \frac{\delta x_f}{\delta \dot{z}_0} \\ \vdots & \ddots & \vdots \\ \frac{\delta \dot{z}_f}{\delta x_0} & \cdots & \frac{\delta \dot{z}_f}{\delta \dot{z}_0} \end{bmatrix} \tag{7}$$

Each entry of the STM provides insight into how an initial perturbation to the state alters the downstream flow. The goals of the differential corrections strategy are to target the reference *x*-component of velocity (v_x, or equivalently, $\dot{x}_f$), and the target perilune passage time, t_p, in the Earth-Moon rotating frame. First, the OMM direction that corrects v_x is explored. The epoch of the target is at the perilune 6.2 revolutions ahead in the NRHO, i.e., t_f. Since the method is strictly targeting $\dot{x}_f$ along the reference trajectory, the corrections algorithm aims to achieve the following perturbation vector,

$$\delta\bar{x}_f = [\delta x_f \quad \delta y_f \quad \delta z_f \quad 0 \quad \delta\dot{y}_f \quad \delta\dot{z}_f]' \tag{8}$$

As the corrections algorithm aims to reduce the error in $\dot{x}_f$, insight is gained by analyzing the initial perturbation from the reference $(\delta\bar{x}_i)$. The initial perturbation is a function of initial error in state and time, as well as the maneuver applied by the OMM. An expression for the initial perturbation is written as,

$$\delta\bar{x}_i = \delta\bar{x}_e + \delta\bar{x}_{OMM} + \delta t_e \begin{bmatrix} \delta\dot{x}_e + \dot{x}_{OMM} \\ \delta\dot{y}_e + \dot{y}_{OMM} \\ \delta\dot{z}_e + \dot{z}_{OMM} \\ \delta\ddot{x}_e \\ \delta\ddot{y}_e \\ \delta\ddot{z}_e \end{bmatrix} \tag{9}$$

The initial perturbation equals the sum of the initial error in state, the maneuver applied, and an updated error due to the difference in phase. The values $\delta\dot{x}_e$, $\delta\ddot{y}_e$, and $\delta\ddot{z}_e$ represent the error in acceleration at the initial time. To account for an error in time, the velocity and acceleration components of the state are multiplied by the change in time to get an approximation for the spacecraft state at the desired epoch. As the STM is computed from the reference trajectory, the error in time is approximated by an error in state due to the timing difference. As the goal is to compute an OMM that meets the constraints of the differential corrections algorithm, the STM can be simplified to depict only variations in v_x, or $\dot{x}_f$. The fourth row of the STM becomes,

$$\Phi_{\dot{x}} = [\Phi_{\dot{x},r} \quad \Phi_{\dot{x},v}] \tag{10}$$

The term $\Phi_{\dot{x},r}$ is a three-dimensional row vector that describes the deviation in the final x-velocity due to a perturbation in initial position components, i.e., $\Phi_{\dot{x},r} = \left[\frac{\delta\dot{x}_f}{\delta x_0} \quad \frac{\delta\dot{x}_f}{\delta y_0} \quad \frac{\delta\dot{x}_f}{\delta z_0}\right]$, whereas $\Phi_{\dot{x},v}$ is also a three-dimensional row vector that maps the initial velocity components to $\dot{x}_f$, i.e., $\Phi_{\dot{x},v} = \left[\frac{\delta\dot{x}_f}{\delta\dot{x}_0} \quad \frac{\delta\dot{x}_f}{\delta\dot{y}_0} \quad \frac{\delta\dot{x}_f}{\delta\dot{z}_0}\right]$. Combining the vectors selected from the STM with the initial perturbation yields,

$$\delta\dot{x}_f = 0 = \Phi_{\dot{x}}\delta\bar{x}_e + \Phi_{\dot{x}}\delta\bar{x}_{OMM} + \delta t_e \Phi_{\dot{x}} \begin{bmatrix} \delta\dot{x}_e + \dot{x}_{OMM} \\ \delta\dot{y}_e + \dot{y}_{OMM} \\ \delta\dot{z}_e + \dot{z}_{OMM} \\ \delta\ddot{x}_e \\ \delta\ddot{y}_e \\ \delta\ddot{z}_e \end{bmatrix} \tag{11}$$

Combining terms then yields,

$$\delta\dot{x}_f = 0 = \Phi_{\dot{x}}(\delta\bar{x}_e + \delta t_e \delta\dot{\bar{x}}_e) + (\Phi_{\dot{x},v} + \delta t_e \Phi_{\dot{x},r}) \begin{bmatrix} \dot{x}_{OMM} \\ \dot{y}_{OMM} \\ \dot{z}_{OMM} \end{bmatrix} \tag{12}$$

The expression illustrates how the numerical corrections algorithm aims to reduce the downstream error in *x*-velocity. It is important to remember that the terms from the STM are dependent on the location of the OMM and the target perilune that is selected (t_f). When the timing error is negligible, the problem is a function of the state error and the STM. The product between the row and column vectors $\Phi_{\dot{x}}\delta\bar{x}_e$ results in a scalar quantity. With three free variables and one constraint, the problem is under-determined, and an infinite number of solutions exist, although the aim for orbit maintenance is to identify propellant-efficient solutions. The product of $\Phi_{\dot{x},v}$ and the OMM maneuver is equivalent to the dot product of the two vectors. As $\Phi_{\dot{x},v}$ is fixed, the linear prediction for the minimum OMM magnitude occurs when the OMM is aligned with either the positive or negative $\Phi_{\dot{x},v}$ direction. Hence when the timing error is small, the linear estimate predicts the OMM burn direction to be along $\Phi_{\dot{x},v}$. Whereas when the timing error is non-negligible, the targeting problem is reliant on several components of the STM and error vectors. With a deviation in phase from the reference, the OMM has additional control on the downstream x-velocity. The combined timing error and maneuver introduces control along the vector $\Phi_{\dot{x},r}$. However, with the added phasing error, the state error is added to velocity and acceleration error, i.e., $(\delta\bar{x}_e + \delta t_e \delta\dot{\bar{x}}_e)$, making the timing error inseparable from state errors. Given the influence of the timing error, the added errors with the subcomponents of the STM $\Phi_{\dot{x},r}$ provide insight into the possible OMM burn directions.

Another perspective for the consideration of OMM directions is based on the dynamics of the NRHO itself. The stable and unstable directions associated with the periodic NRHO defined in the CR3BP offer insight into the OMM directions. The stable and unstable directions again rely on the STM associated with the NRHO. The STM of a periodic orbit evaluated after one full period is known as the monodromy matrix. This matrix relates variations in the state at the initial time to the variations in the state after one period; the STM then represents a stroboscopic map that reduces the continuous system to a discrete-time system. The eigenvalues of the monodromy matrix yield information about the stability of the periodic orbit, and its eigenvectors characterize behavior in the vicinity of the orbit. The monodromy matrix of the 9:2 NRHO has two real eigenvalues λ_i with non-unity magnitude; the eigenvector associated with $|\lambda_i| > 0$ defines the unstable direction, while the eigenvector corresponding to $|\lambda_i| < 0$ defines the stable direction; perturbations in these

two directions result in trajectories that asymptotically depart and approach the NRHO, respectively. It was noted in the operation of the ARTEMIS spacecraft, which flew in unstable Earth-Moon halo orbits, that the optimal OMM directions were aligned with the position component of the stable eigenvector.[10] Thus, the stable direction associated with the NRHO is explored to characterize the behavior of OMMs in the NRHO.

The OMM directions computed by the targeting algorithm are now compared to the burn directions associated with the STM as well as the stable and unstable directions. The burn directions associated with 100 Monte Carlo trials, each with a 3-year duration, appear in *x*-*z* and *x*-*y* projections in the Earth-Moon rotating frame in Figure 4. Several vectors are marked in Figure 4a. The dotted blue vector represents the direction associated with the position components of the stable mode of the NRHO, while the dotted red vector represents the position components of the unstable mode. The green and yellow vectors describe the linear approximation that relates the OM burn Δv with changes in v_x and t_p, respectively, at the target time 6.2 revolutions downstream. The green vector corresponds to the vector $\Phi_{\dot{x},v}$ within the STM. The yellow vector is constructed by projecting the components of $\Phi_{\dot{x},r}$ onto a plane defined by the instantaneous velocity of the orbit and the stable mode. Each of these 4 vectors is computed in the CR3BP, while the OMMs themselves are computed in the ephemeris model. Note the close alignment of the stable direction and the v_x correction direction computed from the STM. Note also that the burn directions plotted in Figure 4a are divided into two groupings. The burns that primarily correct errors in the v_x target, depicted in cool colors, are generally aligned with the stable mode and the green v_x-correction vector computed from the STM. Maneuvers that also correct t_p, depicted in warm colors, include components aligned with the yellow phasing vector computed from the STM. In both cases, the burn may be oriented in either the positive or negative sense along the vector, depending on the errors built up in the orbit over the previous revolution. Alignment of the v_x correction burns with the NRHO stable mode is consistent with optimal OM burn directions observed in the ARTEMIS mission.[10] Note the general directions of the burns in the Earth-Moon rotating frame in Figure 4. For OMMs located at TA = 200°, the OMM lie primarily in the rotating *x*-*z* plane. This behavior is clearly apparent in the 3D projection in Figure 4c. In the 3D projection, the OMM unit vectors are colored according to the NRHO revolution associated with each OM burn in a 9-revolution sequence. The burns that primarily correct v_x are grouped in 9-revolution patterns, but there is no apparent pattern based on geometric revolution number in the burn directions that also target t_p.

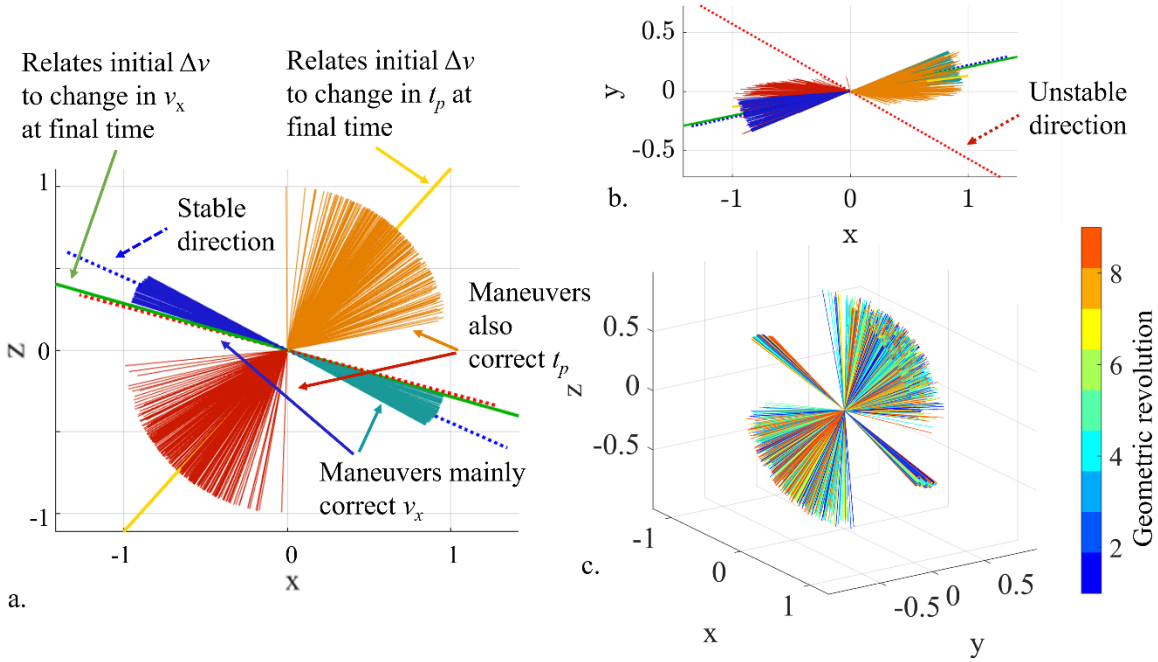

Figure 4. OMM unit vector directions in Earth-Moon rotating coordinates. *x*-*z* projection (a), *x*-*y* projection (b), and 3D view (c).

The patterns in the burn directions change as the tolerance on t_p is varied in the OMM targeter. Not surprisingly, with a tighter tolerance on t_p, more burns contribute to corrections in the perilune passage time,

while, with a wider tolerance on t_p, more burns correct errors only in v_x. It is interesting to note that if the t_p target is relaxed to 6 hours, all of the OM burns are aligned with the stable mode direction in a 1-year simulation. Similarly, tightening the tolerance on the t_p target from 15 minutes to 30 seconds results in a filled-in disk of burn directions: all of the OM burns partially target t_p. These differences are apparent in Figure 5; each subplot represents 100 Monte Carlo trials, each with a 1-year duration. The stable direction is plotted as a dark blue line, and the phasing vector from the STM appears as a yellow line.

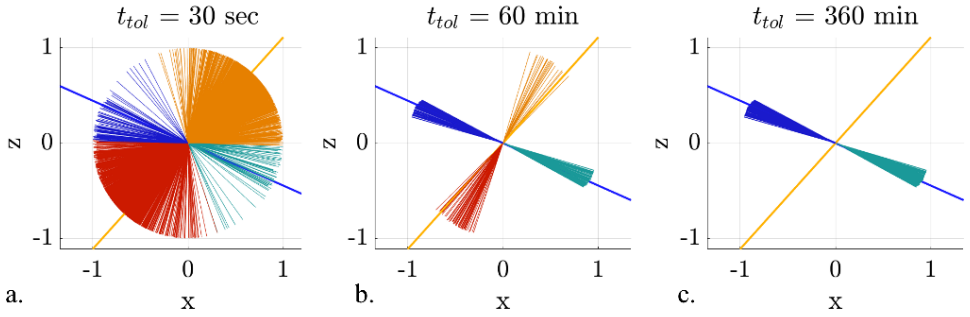

Figure 5. OMM unit vectors in Earth-Moon rotating coordinates varying tolerance on t_p.

Changing the location of the OMM along the NRHO results in a different set of OMM directions. This dependency is not surprising, since the STM and the stable direction all change as a function of TA. The OMM unit vectors appear in Figure 6 for five values of burn TA in *x*-*z* projections (top plots) and *x*-*y* projections (bottom plots). Note that the phasing vector from the STM, plotted in yellow, collapses into the *x*-*y* plane along with the stable (blue) and unstable (red) directions. This collapse may help explain why targeting t_p from apolune is more expensive over short-term simulations and ineffective in long-term simulations.

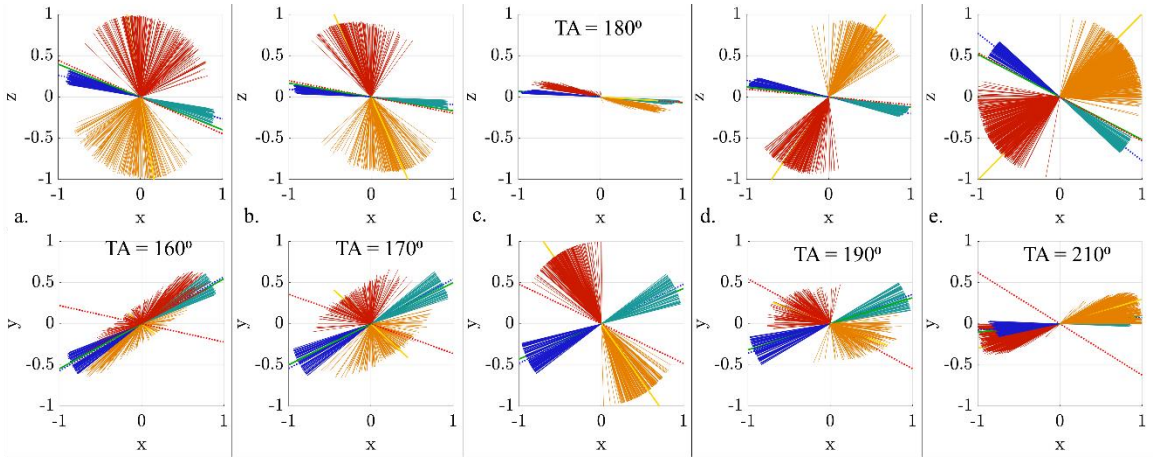

Figure 6. OMM unit vectors varying burn TA. *x*-*z* projections (top) and *x*-*y* projections (bottom).

The targeting horizon selected in this analysis results in OMMs that target the baseline values of v_x and t_p approximately 6.2 revolutions downstream. Adjusting the targeting horizon has a smaller effect on OMM direction as compared to adjusting the burn location or the targeting tolerances. While the STM does depend on the targeting horizon, the stable mode direction does not change, so a greater consistency in burn direction is not surprising. In Figure 7, OMM unit vectors from three simulations are overlaid; OMM directions resulting from 100 56-revolution Monte Carlo trials are plotted in green for a targeting horizon of 2.2 revolutions, in red for a targeting horizon of 4.2 revolutions, and in blue for the standard targeting horizon of 6.2 revolutions. While differences are apparent, note the general agreement in OMM unit vectors across the three simulations. Note that for a targeting horizon of 1.2 revolutions downstream, the maneuver direction is more closely aligned with the most stretching direction, and the algorithm diverges. A 1.2-revolution horizon is ineffective using the current *x*-axis crossing algorithm.[3, 12]

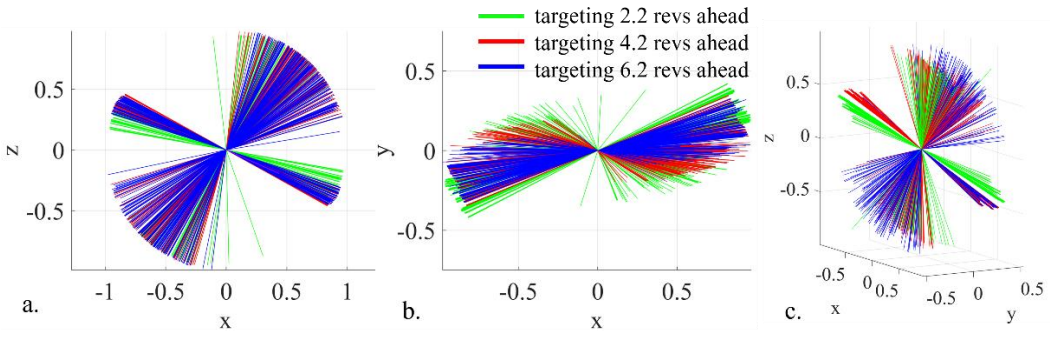

Figure 7. OMM unit vectors varying targeting horizon.

The burn directions are further investigated by exploring the errors in the targeting parameters, v_x and t_p, at the target perilune 6.2 revolutions downstream. The OMMs depicted in Figure 4 are sorted according to the magnitude of the errors relative to the baseline NRHO at the targeting horizon and plotted in Figure 8. The coloring scheme matches that in Figure 4, where the burns that primarily correct v_x are colored in shades of blue, while the OMMs that also correct t_p are colored in red and orange. Figure 8a indicates the burn directions along with the v_x errors at the target 6.2 revolutions downstream. The blue curves illustrate the maneuvers along the stable mode. Note that when the v_x error is near zero, the OMMs along the stable mode fall below the 3 cm/sec threshold, and a gap appears in the data. However, the maneuvers that correct phasing errors, in red and orange, persist through the regions of low v_x error. Conversely, Figure 8b indicates the burn directions along with the t_p error at the target 6.2 revolutions downstream. Comparing the maneuvers along the stable direction (cool colors) with the maneuvers along the t_p direction (warm colors), only maneuvers aligned with the stable mode occur when the t_p error is within the 15-minute threshold, as denoted by two horizontal black lines. The maneuver magnitudes for each set of maneuvers appears in Figure 8c. Again, the OMMs along the stable mode are plotted in cool colors, and the OMMs aligned with the phasing vector appear in warm colors. The larger magnitudes associated with the warm colors reveal that OMMs along the stable mode tend to be smaller in magnitude. In each of the plots in Figure 8, the points are sized to scale with the magnitude of the maneuver; not surprisingly, maneuvers that correct smaller errors are smaller in magnitude.

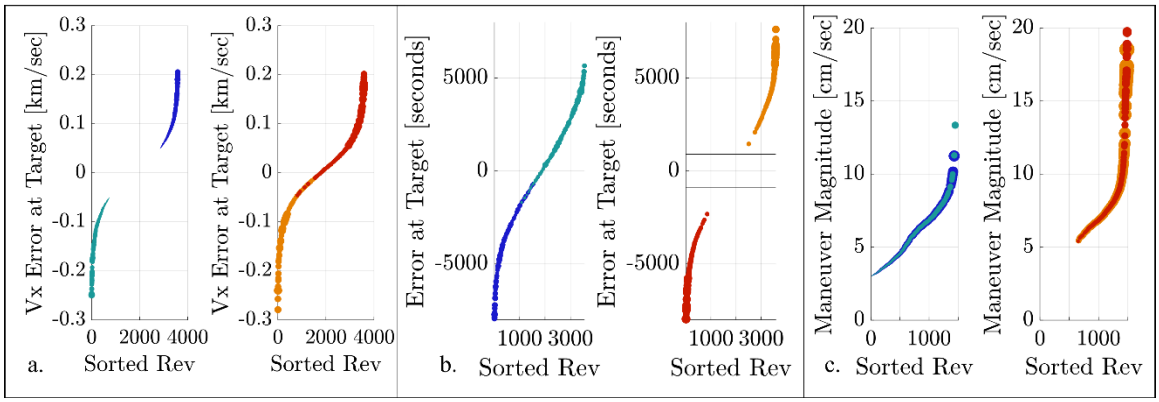

Figure 8. Errors in v_x (a), errors in t_p (b) at the target perilune, and OMM magnitudes (c), for burns that correct v_x (cool colors) and t_p (warm colors).

The same set of OMM data is plotted again in Figure 9 to relate the error values as measured at the target and at the OMM location to the resulting maneuver. In Figure 9a, the value of each v_x error at the target plotted against the t_p error at the target. In this plot, four regions emerge, with the OMMs that correct v_x and t_p forming distinct clusters. The area near the origin correlates to small errors from the reference; resulting OMMs have magnitudes below the 3 cm/s threshold and are not executed or plotted. Again, the size of each datapoint is scaled by the maneuver magnitude so that larger maneuvers are marked with larger points in the plot. Clearly, the further the spacecraft is from the baseline in v_x and t_p at the target, the higher the magnitude of the resulting maneuver. Similarly, the data plotted in Figure 9b relates the error at the OMM location, in

this case at TA = 200º, to the resulting maneuver patterns. A linear prediction of the downstream variation is generated by leveraging components of the STM; specifically, $\Phi_{\dot{x}}$ as defined in Equation 10. Multiplying the row vector $\Phi_{\dot{x}}$ by the error column vector $\delta\bar{x}_e$ provides a scalar estimate of the error in the downstream value of v_x. These predicted errors in v_x are plotted as a function of the timing or phase error at the OMM location in Figure 9b. While the patterns are not as distinct as in Figure 9a, clear trends are visible. A positive predicted error in v_x corresponds to a correction along the associated vector aligned with the stable mode (in dark blue) while a negative error in v_x leads to a maneuver direction in the opposite direction (light blue). Similarly, positive and negative initial errors in t_p tend to lead to maneuvers directed along the corresponding phasing vector (in red and orange, respectively.) A correspondence between the error magnitude and the maneuver size, as signified by the width of each datapoint, is not clearly apparent in Figure 9b.

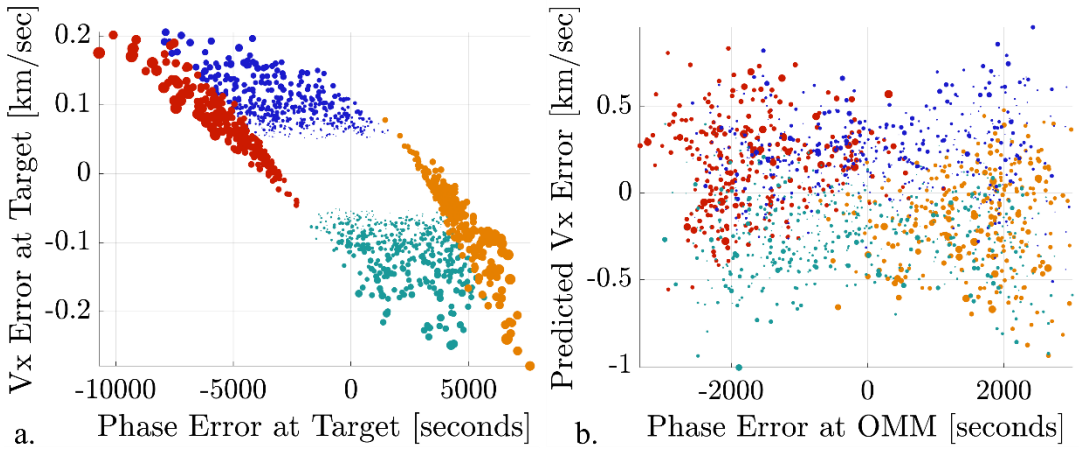

Figure 9. Maneuver magnitudes (a) for maneuvers that correct v_x (cool colors) and t_p (warm colors). Downstream error magnitude in v_x vs t_p (b).

The OMM directions illustrated in Figure 4 - Figure 7 are represented in Earth-Moon rotating coordinates and, thus, do not yield information regarding attitude or solar incidence during the OM burns. However, OMM attitude relative to the Sun may be of interest when thermal or other constraints are considered. Because the 9:2 NRHO is fixed relative to the Earth-Moon line, and the Sun rotates around the Earth-Moon system once per synodic month, the burn directions follow a 9-revolution pattern when viewed in a Sun-relative frame. These 9 geometric revolutions are denoted by a Moon angle, defined as the angle between the positive x-axis in the Sun-Earth rotating frame and vector from the Earth to the Moon. A polar plot representing the Moon angle at TA = 200º as a function of elapsed years for each of the 9 revs appears in Figure 10a. The "spokes" in the polar plot are numbered in time-sequence; the NRHO completes a full cycle in steps of 80º, with 40º between each "spoke", so that rev 6, for example, lies between revs 1 and 2 in the polar plot. These 9 geometric revs characterize the burn directions when viewed in a Sun-relative frame. The NRHO in Figure 1 is colored according to the same scheme, with each colored revolution commencing from the OMM location at an osculating TA = 200º.

Burn directions from a 300-trial Monte Carlo simulation with a duration of 2 years appear in Figure 10b in a Sun-relative reference frame where the Sun-direction is designated by the origin, and azimuth and elevation relative to the Sun-vector are represented by the horizontal and vertical axes respectively. Each burn direction is colored according to its geometric revolution number along the nine characteristic revolutions of the 9:2 NRHO. Note that the burns are clustered in groups. The individual OMM orientations are marked by small dots, while the centroid of each group is marked with a large triangle; for illustration, the OM burns associated with one particular revolution of the nine, denoted "rev 4", are circled. The burn directions circled in shades of blue primarily correct errors in v_x, while the burns outlined in red and orange also correct errors in t_p. Since the OMMs can be oriented in either the positive or negative sense, two groups appear for each type of burn. Note that while burns with zero or 90º elevation are rarely observed, a near-continuum of azimuth values occur. The mean value of the positive and negative vectors corresponding to the stable direction and the phasing/t_p correction direction derived from the STM are plotted as blue and

yellow asterisks, respectively, for each revolution on the plot. Note the agreement between the centroid of the OMM directions and the stable/phasing vectors.

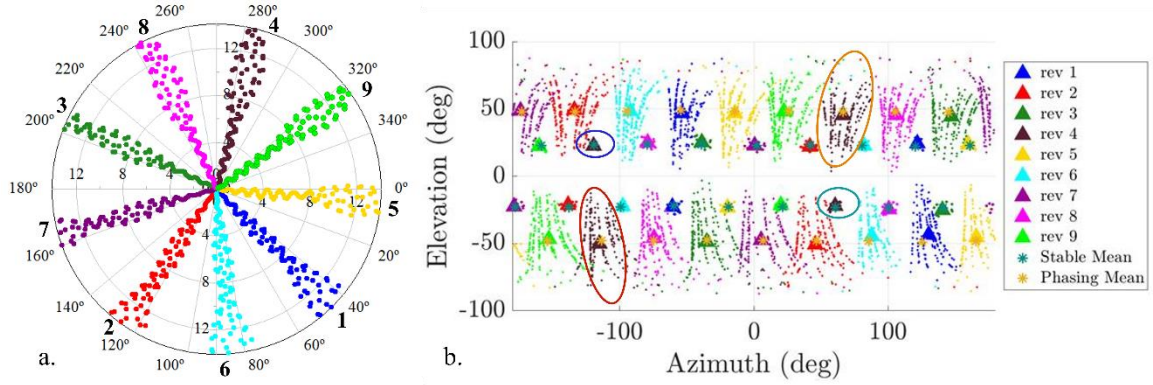

Figure 10. Polar plot of Moon angle over time of 9 geometric NRHO revs (a), Scatter plot of OMM directions (azimuth and elevation) relative to the Sun vector (0,0) for the 9 revs (b).

When the tuning parameters associated with the OM algorithm change, the orientation of the OMMs with respect to the Sun also vary. For example, consider the OMM directions relative to the Sun for three maneuver locations along the NRHO: TA = 160º, TA = 180º, and TA = 200º. Pictured in Figure 11 for Monte Carlo simulations of 100 two-year trials, the individual OMM orientations are marked by small dots, while the centroid of each group is marked with a large triangle. As observed in Figure 6, changing the TA of the OMM alters the characteristics of the burn directions, and the OMMs tend to collapse into the Earth-Moon orbital plane at TA = 180º. This collapse is also observed in Figure 11b, with OMM elevation values approximately equal to zero. However, the azimuth relative to the Sun also changes as both the directions and epochs of the maneuvers vary. The azimuth and elevation of two maneuver direction centroids are plotted as a function of OMM TA in Figure 12. These two curves show the evolution of burn direction as the location of the burns shift along the NRHO for the OMMs that correct errors in v_x. These curves are associated with one specific characteristic revolution; specifically, the revolution labeled "rev 4" in Figure 11. The azimuth of the centroid of the OMMs varies from maximum values of +/- 101º at TA = 150º to +/- 60º at TA = 200º. This variation is a function of the changing maneuver directions as well as the differences in maneuver epoch as the TA is varied. If a given attitude, particularly in azimuth, is undesirable for a given spacecraft configuration, for example, for thermal reasons, adjusting the location of the OMM along the NRHO may offer operational flexibility. Note that the burns that correct the NRHO phase also vary in direction as a function of OMM location along the NRHO; however, as the burns collapse into the Earth-Moon plane near apolune, the centroids for the phasing OMMs become less well defined. Recall that in the short term, targeting both vx and tp from TA = 180º is more expensive, and over the long term, TA = 180º is an ineffective location for OMMs that maintain the eclipse-favorable phase. These limitations must be considered when selecting an OMM location.

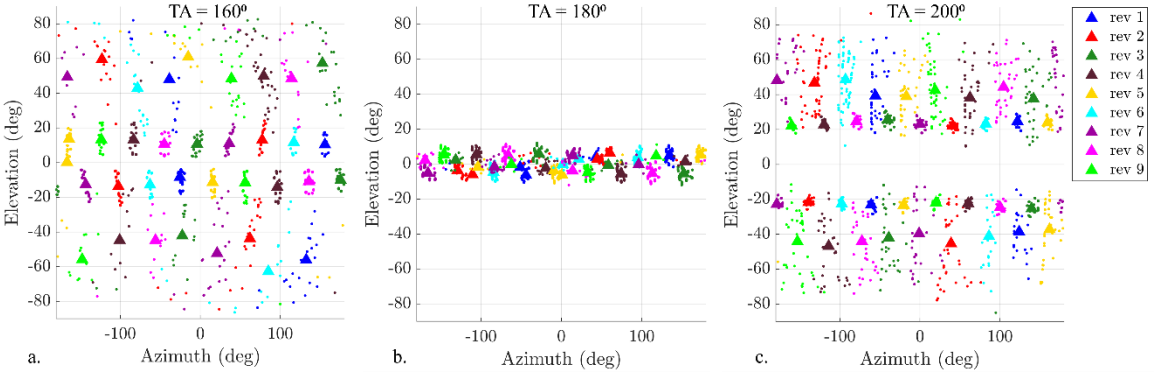

Figure 11. Sun-relative burn directions for three TA values.

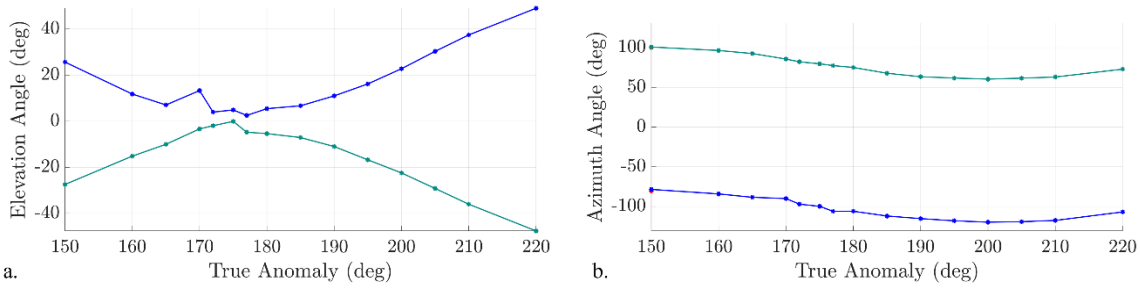

Figure 12. Azimuth (a) and elevation (b) of the maneuver direction centroids for geometric "rev 4" as a function of OMM TA.

ORBIT MAINTENANCE ALGORITHM TUNING

The tuning parameters outlined in Table 2 consist of the location of the burn along the NRHO, parametrized by osculating true anomaly, the targeting tolerances on both v_x and t_p, the weighting parameter used in the t_p targeting process, the minimum OMM magnitude threshold for execution, and the targeting horizon. Each of these parameters affects OM performance.

The placement of the OM burns affects both the cost and reliability of the OM algorithm. The NRHO is highly sensitive near perilune, so burns near the Moon magnify orbit determination and maneuver execution errors. Additionally, orbit determination (OD) state errors are larger near perilune, so if the spacecraft state as measured near perilune is used to plan maneuvers, costs increase as well. Thus, the OM burns are located along the NRHO away from perilune. A previous investigation[3] identifies the lowest cost location for an OMM when only v_x is targeted, without maintaining the eclipse-favorable phase, at apolune precisely. Burns directly at TA = 180º, on the other hand, are more expensive in the short term, and are ineffective over longer propagations, when both v_x and t_p are targeted. Instead, burns on either side of apolune achieve better performance. The behavior then depends on operational constraints, including the data cutoff for the orbit determination state. In practice, for a spacecraft that is not operating autonomously, ground-based measurements from the Deep Space Network or other antennas are processed to determine the position and velocity of the spacecraft prior to the targeting process. A finite duration is required for the operations team to receive the data, compute the OD solution, design the maneuver, and upload it to the spacecraft. The maneuver is, thus, designed based on a spacecraft state propagated from the OD data cutoff time to the maneuver epoch. This data cutoff time effects the preferred placement of the OM burns.

The mean annual OM cost for an uncrewed spacecraft as a function to OM burn TA appears in Figure 13a for two scenarios: in blue, a 24-hour OD data cutoff is assumed, and in orange, a 4-hour OD data cutoff is implemented. Each datapoint represents the mean annual Δv resulting from a 100-trial, one-year Monte Carlo simulation. Two local minima appear in the plots. The first, centered at approximately TA = 160º, yields the lowest cost for a 4-hour OD data cutoff. However, with a 24-hour data cutoff, the spacecraft state for an OMM at TA = 160º is measured near perilune. The increased sensitivity and degraded OD state knowledge near perilune means that placing an OM burn at TA = 160º is ineffective when the OD data cutoff is 24 hours prior to the OM burn. The second local minimum is centered at TA = 200º. In this case, both data cutoff options result in the final OD state measured after apolune, and the OM burn is effective in both cases. Note the relatively flat nature of the curve near the minimum values at TA = 160º and TA = 200º. This flat behavior leads to flexibility in OM burn placement or timing that may be useful for operations within this 6.5-day orbit, for example, to ensure OM burn execution always occurs during day-shift operations. It is important to note that burns placed directly at apolune, TA = 180º, are expensive and are not effective long-term when t_p targets are included to maintain the eclipse-favorable phase.

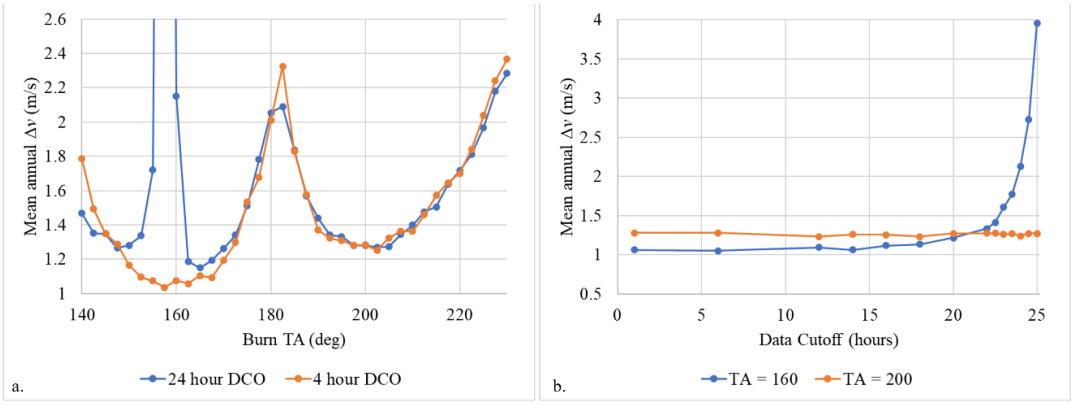

Figure 13. Mean annual OM Δ*v* as a function of OMM TA for two data cutoff values (a) and as a function of OD data cutoff for two OMM TA values (b).

The relationship between OM burn placement and data cutoff is further explored in Figure 13b. Again, each datapoint represents the mean annual Δ*v* resulting from a 100-trial, 56-revolution Monte Carlo simulation. In this case, the blue curve represents OM burn placement at TA = 160º while the orange curve represents OMM placement at TA = 200º. Note that for OD data cutoffs under 20 hours, the mean annual cost is lower with burns placed at TA = 160º. For OD data cutoff times over 20 hours, the cost increases dramatically as the data cutoff location approaches perilune and burns cease to be effective. In contrast, the cost when the burns are placed at TA = 200º is relatively constant, since the data cutoff values explored here do not result in states measured near perilune. Approximate locations of TA = 160º and TA = 200º along the NRHO, as well as a data cutoff 24 hours prior to each TA, are marked in Figure 14.

Another operational consideration that affects burn TA selection is the ability to pre-plan the OMM attitude and magnitude well in advance of the burn execution for validation. For an accurate maneuver design, the OD state used in the design must be computed including tracking data collected after perilune passage. A maneuver at TA = 160º occurs approximately 26 hours after perilune passage: the available time between perilune passage and burn execution at TA = 160º is insufficient for the generation of preliminary burn designs. Conversely, the spacecraft reaches TA = 200º approximately 5.5 days after perilune passage. With a burn placed at TA = 200º, there is sufficient time available for a preliminary maneuver design to be validated before the final maneuver is designed after the OD data cutoff.

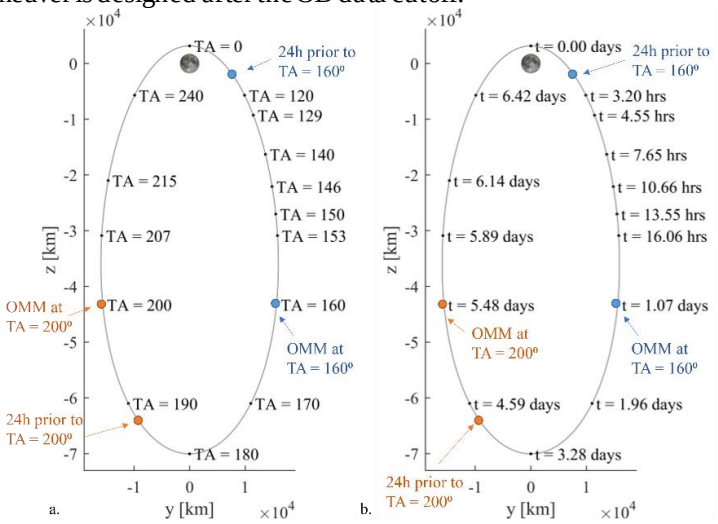

Figure 14. NRHO parameterized by TA (a) and time (b).

Another tuning parameter that affects OM algorithm performance is the minimum maneuver threshold, or the Δ*v* magnitude below which a maneuver is not executed. The selection of this threshold, Δv_{min}, depends on several factors, including the errors present in the modeling as well as, once again, operational

considerations. A higher value of Δv_{min} is appropriate when the errors acting on the spacecraft are larger. As an example, the relationship between the mean annual OM Δv and the minimum maneuver threshold is explored in Figure 15a for varying perturbations associated with reaction wheel desaturations (desats). In orange, the cost is computed assuming 2 desats per revolution: one at perilune and one prior to the OMM. In blue, the simulation assumes 4 desats per revolution, three occurring over perilune and the fourth associated with the OMM. In grey, the costs are computed when 6 desats are executed, five near perilune and the final prior to the OMM. Each data point in the curves represents the mean annual OM Δv after a 300-trial, one year Monte Carlo simulation. It is immediately apparent that, as observed in previous studies,[5,13] the OM cost is sensitive to desat perturbations near perilune. The mean annual cost with 6 total desats increases by over a factor of 1.5 as compared to the mean annual OM cost with only 2 total desats perturbation per revolution. In addition, the minimum in the curve shifts to the right as the perturbations increase. The value of Δv_{min} associated with the lowest mean annual costs shifts from 0.75 cm/s with 2 desats per revolution, to 1 cm/s with 4 desats per revolution, to 1.25 cm/s when 6 desats are experienced per revolution.

The selection of Δv_{min} also depends on operational factors. When a burn is waived, the burden on the operations team on the ground is reduced, slews to OM attitude are not executed, and thrusters are not fired. It may be desirable to waive more burns at the expense of a small amount of added OM Δv. The mean number of waived maneuvers over each 56-revolution simulation is plotted as a function of Δv_{min} in Figure 15b. Again, each datapoint represents the mean value after a 300-trial simulation, and the orange, blue, and grey curves correspond to 2, 4 and 6 total desats per NRHO revolution. The slope in each curve is quite steep for thresholds below 1 cm/s, and the curves flatten as Δv_{min} increases. By selecting a minimum maneuver threshold larger than the value associated with the minimum cost, the number of waived OMMs is increased significantly.

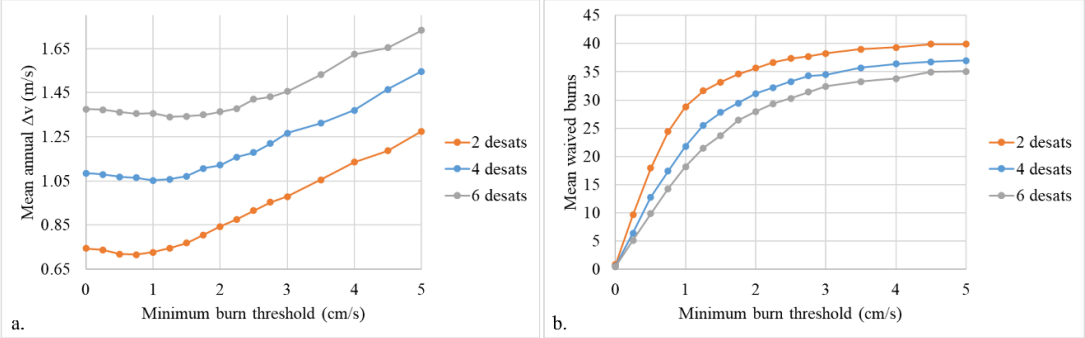

Figure 15. Mean annual OM Δv as a function of minimum burn threshold, Δv_{min}.

As previously mentioned, the selection of targeting horizon has a small effect on the OMM direction; adjusting the horizon also changes the cost. In general, a longer horizon tends to yield lower cost but increased computation time. The selected targeting horizon must remain shorter than the time it takes the orbit to depart the NRHO in the presence of assumed errors. In the current study, a horizon of 6.2 revolutions is an effective compromise between cost and reliability; if targeting is unsuccessful, the algorithm successively reduces the horizon until the success is achieved, without attempting a horizon of 1.5 revolutions. With the tuning parameters outlined in Table 2, the reduction of horizon is not typically necessary either with error models as outlined in Table 1 or for larger errors associated with crewed spacecraft. The annual OM Δv as a function of targeting horizon appears in Figure 16; each datapoint represents 100 one-year Monte Carlo trials.

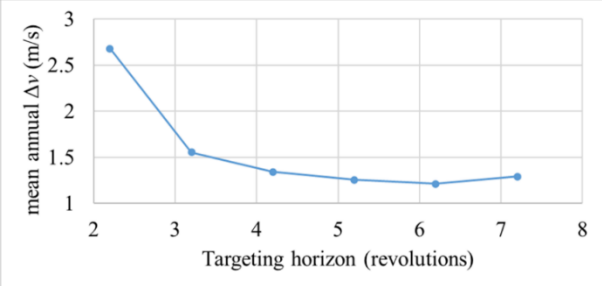

Figure 16. Mean annual OM Δv as a function of targeting horizon.

LONG-DURATION ORBIT MAINTENANCE AND ERROR DAMPING

The Gateway is planned to remain in cislunar space for a 15-year lifetime. Thus, it is important to consider long-term behavior of the OM algorithm. Results from a single Monte Carlo trial for 820 revolutions appears in Figure 17, assuming algorithm parameters as outlined in Table 2. The cumulative Δv follows a smooth curve (albeit with a slightly increasing slope), and the individual OMM Δv magnitude values remain under 20 cm/s, as illustrated in Figure 17a and b, respectively. However, after several years in the NRHO, the frequency of variations in the perilune passage time deltas relative to the baseline increase, and the position deltas, particularly in the rotating y and z directions, begin to exhibit secular growth. While no convergence problems in the targeter are observed in Monte Carlo simulations, such growth in the z-component of the position vector leads to complications, including larger variations in perilune altitude than desired. A 50-trial simulation yields a mean annual OM cost of 1.35 m/s, with minimum and maximum costs of 1.1 m/s and 1.6 m/s respectively.

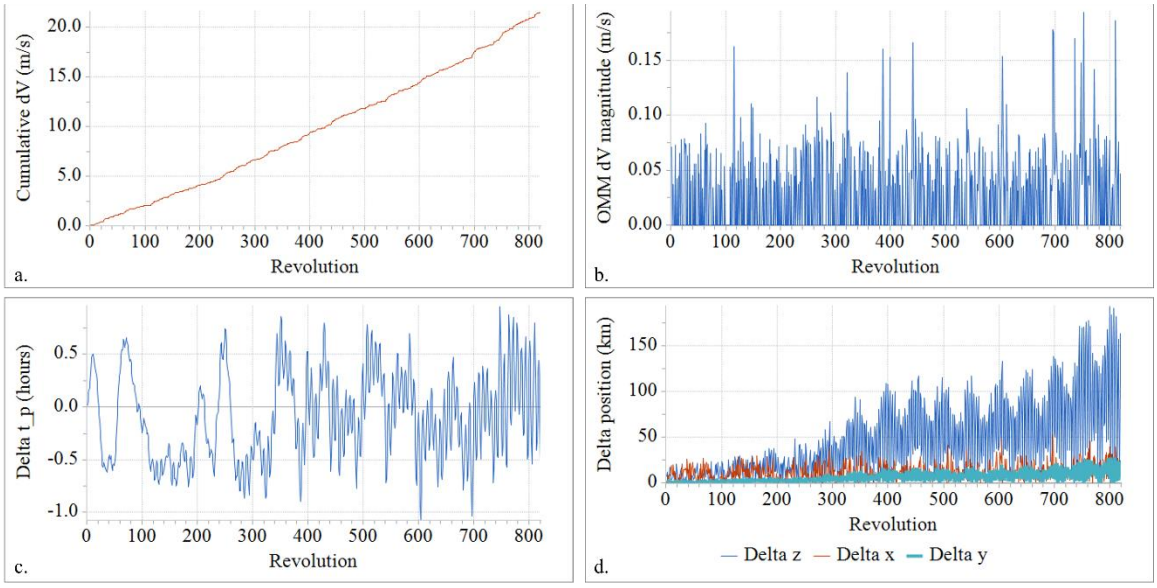

Figure 17. Single 15-year simulation without additional damping.

To mitigate this secular growth in the position deltas relative to the baseline NRHO, and to damp the oscillations in the perilune passage time deltas, a strategy is adopted based on a technique originally introduced in previous analyses incorporating corrections to orbit perturbations.[7] A trigger is set at a particular position delta threshold, and when reached, an additional target is added to the OM burn for one or more revolutions after the trigger is tripped. Through a large set of Monte Carlo simulations exploring a variety of triggers, targets, tolerances, and repetitions of the augmented OMM target, an effective set of parameters is identified:

- Trigger: rotating y-position delta > 10 km at previous perilune passage
- Additional target: achieve y-position delta < 1 km at perilune passage 6.2 revolutions downstream
- Repetition: additional target executed for a single OMM after the trigger is tripped

The augmented OM algorithm successively targets first v_x, then v_x and t_p, and finally v_x, t_p, and y to compute the OMM Δv during the revolution following the tripping of the $\Delta y > 10$ km trigger. The additional target results in a larger OMM during that revolution, but the augmented OMM effectively damps the increasing position deltas as well as the high frequency in the perilune passage time deltas. A single representative Monte Carlo trial exhibits the behavior over 820 NRHO revolutions in Figure 18. In this sample trial, the y-position delta threshold of 10 km is triggered twice, first on revolution 269, and then again on revolution 613. In each case, an augmented OMM is executed with magnitude just over 1 m/s. These larger OMMs are visible in both the cumulative Δy plot in Figure 18a as well as in the individual OMM magnitude plot in Figure 18b. The frequency of oscillations in the t_p deltas, pictured in Figure 18c, remains relatively steady. The effects of

the damping OMMs is most apparent in Figure 18d, where the position deltas as measured at perilune drop as a result of the extra *y*-position target in the OMM. This single representative trial has an annual OM Δv cost of 1.35 m/s, including the two larger damping OMMs.

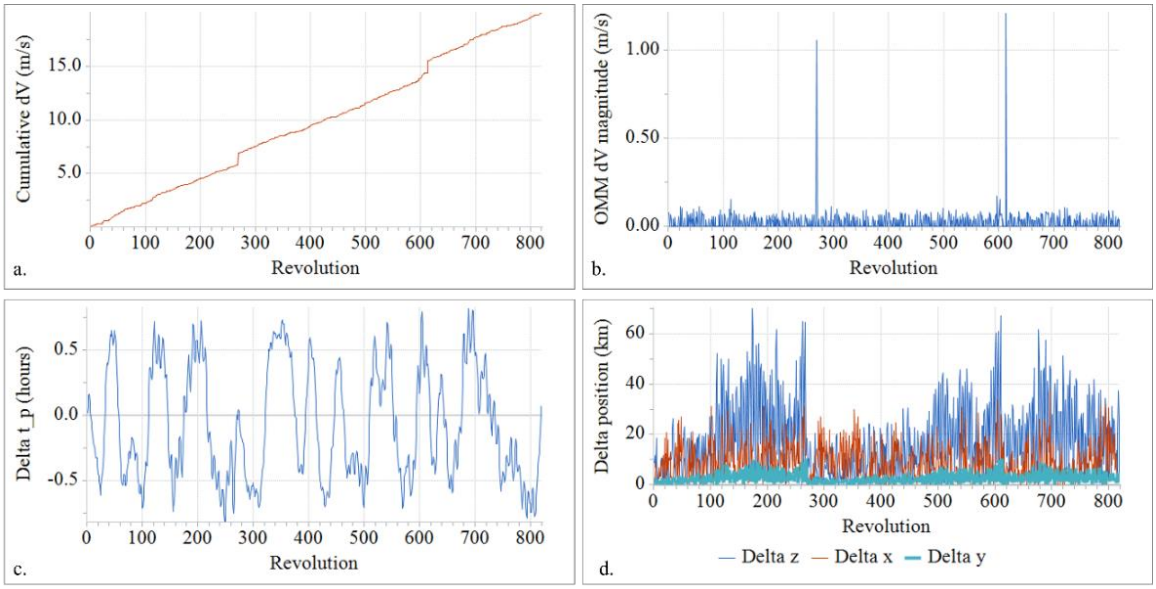

Figure 18. Single 15-year simulation with additional damping.

To confirm these results in the presence of statistical errors, a 50-trial Monte Carlo simulation is executed. The mean annual Δv cost is 1.34 m/s, with a minimum value of 1.2 m/s and a maximum of 1.6 m/s. The simulation yields zero to four damping events per trial, with a mean value of 1.5 damping burns per 820-revolution trial. The results are summarized in Figure 19. Note the lack of secular growth in the deltas relative to the baseline in the perilune position vector components as well as the perilune passage time. The damping algorithm effectively maintains the quiet, uncrewed spacecraft near the baseline NRHO throughout each of the 15-year trials. Steps in the cumulative Δy plot in Figure 19a correspond to the damping events in each individual trial, and the larger OMM costs observed in Figure 19b illustrate that these individual OMMs can reach over 1.2 m/s, while typical OMMs do not exceed 20 cm/s. It is interesting to note that the 15-year costs including the damping events is nearly identical to the 15-year costs when damping events are not included. The increased OM costs associated with diverging from the baseline NRHO balance out the additional costs of the larger damping OMMs. These results corroborate previous studies of OM costs following perturbations.[7]

Note that the secular growth in position deltas is not typically observed during simulations less than three years in duration. Thus, when exploring the long-term effectiveness of a given OM algorithm, it is important to consider results from simulations of the entire mission span. Even in longer simulations, the growth is not always observed: nine of the 50 trials illustrated in Figure 19, or 18%, do not trigger the threshold and, thus, execute no damping OMMs. It is also notable that the increase in position deltas is not observed when the OM location is set to TA = 160º, prior to apolune, as illustrated in a previous analysis.[5] However, as discussed previously, when operational constraints are considered, OMM execution after apolune can be preferable. The damping method outlined here may also be useful to correct for the buildup of inevitable perturbations associated with the construction and operation of a crewed station: docking and undocking perturbations, venting and exercise perturbations, and additional RCS activity for attitude maintenance.

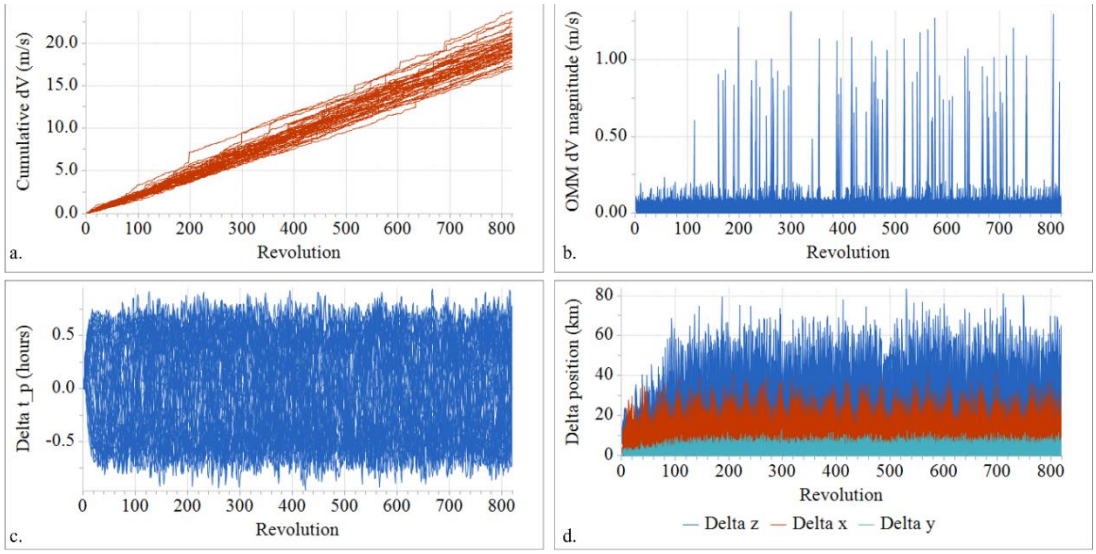

Figure 19. 15-year Monte Carlo simulation: 15 years with additional damping.

As noted, changing tuning parameters in the targeting algorithm affects the results of the simulations. One important observation is that, over long-term, 820-revoltion simulations that include the additional damping when the *y*-trigger is tripped, the OM algorithm performs well for TA ranges between 190º and 210º. That is, the trends observed for shorter propagations, illustrated in Figure 13, hold over 15 years. Thus, flexibility to move the OMM TA to maintain favorable daytime timing for operations is available for long-duration missions. A previous investigation[13] notes that the targeting algorithm is relatively insensitive to the tolerance on v_x; the same results are observed in the current study. The tolerance on t_p targeting, t_{tol}, is coupled with the weighting parameter, W_t. Assuming $W_t = 0.3$, the effects of changing t_{tol} in long-duration simulations is observable in both the OM cost and the deltas in t_p with respect to the baseline NRHO. As illustrated in Figure 19c, the values of t_p remain with about 0.8 hours of the baseline for a mean annual cost of 1.35 m/s when t_{tol} = 15 minutes. When t_{tol} is reduced to 6 minutes, the mean annual OM cost increases slightly to 1.43 m/s; although the number of damping maneuvers observed does not vary significantly, the cost is higher to remain closer to the baseline. The deltas in perilune passage time remain within about 0.5 hours of the baseline throughout the 15-year simulation. When t_{tol} is relaxed to 60 minutes, the cost again rises, with more large damping maneuvers observed over time; deltas in t_p relative to the baseline remain within approximately 2.5 hours. The results of 50 820-revolution Monte Carlo trials appear in Figure 20.

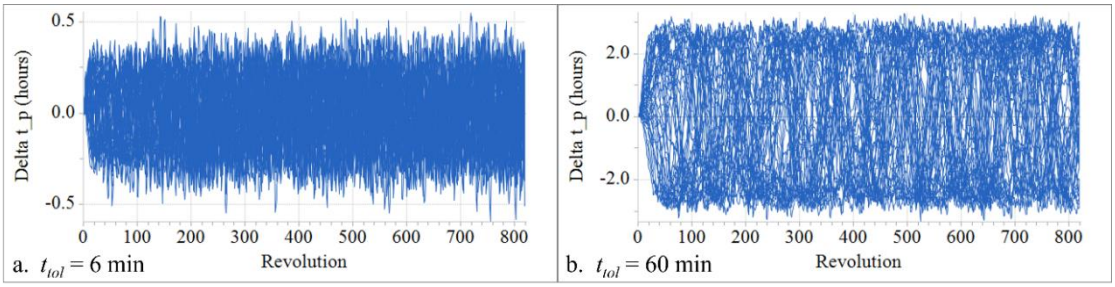

Figure 20. Deltas in t_p relative to the baseline with t_{tol} = 6 min(a) and t_{tol} = 60 min (b).

ORBIT MAINTENANCE INCORPORATING ATTITUDE CONSTRAINTS

For some missions, thermal or communications constraints may lead to attitude preferences or restrictions that limit the time allowed in a given attitude or limit attitude bands entirely from available flight profiles. Consider a scenario in which an attitude that places the thrusters perpendicular to the Sun-vector is undesirable. In this case, OMM directions of +/- 90º azimuth are restricted. A preliminary investigation explores the robustness of the OM algorithm when certain attitude bands are unavailable for OMMs. In this first simple example, a restricted attitude band is defined around an azimuth of +/-90º with respect to the Sun

direction. If an OMM direction lies within this restricted attitude band, the OMM is not performed. Results from example simulations appear in Figure 21. On the left, Figure 21a and Figure 21c represent the OMM directions and the OMM magnitudes in the nominal case with no attitude restrictions. On the right, Figure 21b and Figure 21d plot the same quantities when an attitude constraint of +/-40º is applied around azimuth = 90º and azimuth = -90º. It is immediately apparent from Figure 21b that maneuvers along certain geometric revolutions are generally not executed when the attitude constraint is applied. This figure represents 50 Monte Carlo trials, each 15 years in duration. While there is some spread and overlap in the burn directions associated with each rev, OMMs corresponding to revs 4, 6, and 8 tend to lie within the band of attitude constraints and are waived; these OMMs are associated with Moon angles near 90º and 270º, as observed in Figure 10a. Conversely, OMMs corresponding to revs 1, 2, 3, 5, 7, and 9 are generally allowed. These OMMs avoid Moon angles near 90º and 270º. The OMM magnitude of the burns also illustrate the revs associated with waived maneuvers. Figure 21c and Figure 21d display burn magnitudes resulting from 100 1-year Monte Carlo trials. Without an attitude constraint in Figure 21c, the burn magnitude for each OMM remains under 20 cm/s, and maneuvers are waived at random when burn magnitudes do not reach the minimum threshold of 3 cm/s. In contrast, with the attitude constraint applied in Figure 21d, individual maneuver magnitudes are higher, typically remaining under 30 cm/s, and notably, certain maneuvers are waived in every trial because they violate the attitude constraint. On the other hand, maneuvers that do not violate the attitude constraint rarely, if ever, fall below the minimum magnitude threshold.

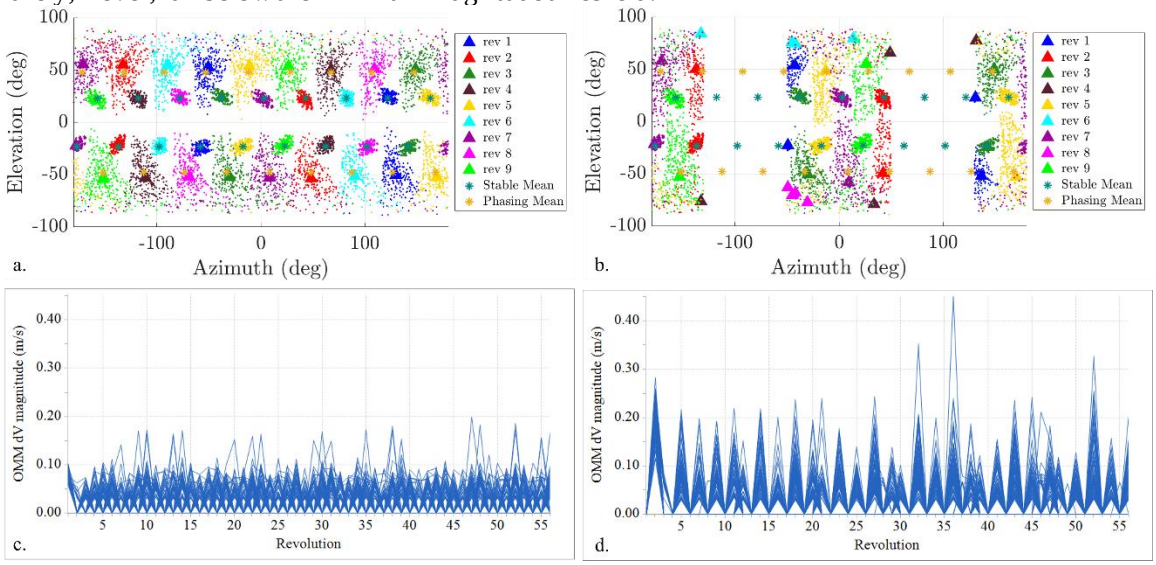

Figure 21. OMM burn directions relative to the Sun-vector (top) and OMM burn magnitudes (bottom) with no attitude constraints (left) and with a +/-40º constraint (right).

The simulations are repeated for a range of attitude restriction bands, each centered around +/- 90º azimuth. For bands of +/-40º and narrower, the algorithm performs nominally: over 300 1-year Monte Carlo trials, each OMM in each trial successfully targets v_x and t_p 6.5 revolutions downstream. For bands of +/-45º and +/- 50º, some revolutions fail to target 6.5 revolutions ahead, but those revolutions successfully target 4.5 revolutions ahead, and each 56-revolution trial completes successfully. The mean annual OM Δv for the simulations appear in Figure 22 as a function of the attitude constraint band width. Unsurprisingly, the cost grows as the constraint band increases, but the algorithm remains robust for uncrewed simulations. Longer Monte Carlo simulations spanning 15 years in duration for 50 trials confirm that for attitude constraints of 40º or narrower, the OM algorithm performs robustly, with no need to reduce the targeting horizon, for a small cost penalty. Recall that from one revolution to the next, the Moon angle at the OMM advances in ~80º steps, as illustrated in Figure 10a. Thus, with an attitude constraint of +/- 40º or narrower, the constraint does not require the algorithm to skip two subsequent OMMs, and algorithm robustness is maintained. Future analyses will expand on this investigation to assess OM algorithm reliability with attitude constraints in the presence of errors associated with crewed missions, such as venting and docking perturbations.

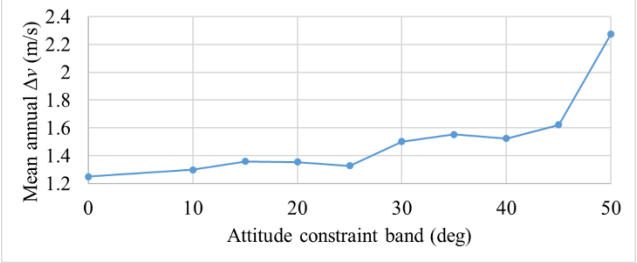

Figure 22. Mean annual Δ*v* as a function of attitude constraint band.

CONCLUDING REMARKS

For a spacecraft operating in NRHO, orbit maintenance is critical for long-term operations. This investigation outlines the current plans for OM of Gateway in its 9:2 NRHO, exploring various parameters and details that affect the cost and behavior of the orbit maintenance algorithm. The maneuver magnitudes and directions are explored over long-term Monte Carlo simulations. The effects of a minimum maneuver threshold are demonstrated, annual OM cost is computed as a function of maneuver location along the NRHO, and the dependence of acceptable maneuver locations on OD data cutoff is illustrated. The relationship between burn direction and annual cost and tuning parameters in the targeting algorithm, e.g. the weighting factor W_t and the tolerances v_{tol} and t_{tol}, are explored.

Operational constraints could limit desirable attitudes for orbit maintenance burns. The effects of burn attitude constraints on the cost and reliability of the OM algorithm are explored in the current investigation, and long-term behavior in the NRHO for an uncrewed, quiet spacecraft is considered. When differences in the spacecraft position vector with respect to the NRHO baseline begin to grow beyond acceptable limits, a damping maneuver is introduced to effectively limit error growth.

ACKNOWLEDGMENTS

The authors would like to thank Brian McCarthy, Connor Ott, and Ethan Kayser for insightful discussions. Portions of this work were completed at NASA JSC through contract #NNJ13HA01C and through the USRA program.

REFERENCES

[1] Zimovan, E., K. C. Howell, and D. C. Davis, "Near Rectilinear Halo Orbits and Their Application in Cis-Lunar Space," 3rd IAA Conference on Dynamics and Control of Space Systems, Moscow, Russia, May-June 2017.

[2] Davis, D. C., S. A. Bhatt, K. C. Howell, J. Jang, R. L. Whitley, F. D. Clark, D. Guzzetti, E. M. Zimovan, and G. H. Barton, "Orbit Maintenance and Navigation of Human Spacecraft at Cislunar Near Rectilinear Halo Orbits," 27th AAS/AIAA Space Flight Mechanics Meeting, San Antonio, Texas, February 2017.

[3] Guzzetti, D., E. M. Zimovan, K. C. Howell, and D. C. Davis, "Stationkeeping Methodologies for Spacecraft in Lunar Near Rectilinear Halo Orbits," AAS/AIAA Spaceflight Mechanics Meeting, San Antonio, Texas, February 2017.

[4] Newman, C. P., D. C. Davis, R. J. Whitley, J. R. Guinn, and M. S. Ryne, "Stationkeeping, Orbit Determination, and Attitude Control for Spacecraft in Near Rectilinear Halo Orbit," AAS/AIAA Astrodynamics Specialists Conference, Snowbird, Utah, August 2018.

[5] Davis, D. C., F. S. Khoury, and K. C. Howell, "Phase Control and Eclipse Avoidance in Near Rectilinear Halo Orbits," AAS Guidance, Navigation, and Control Conference, Breckenridge, Colorado, February 2020.

[6] Thompson, M. R., M. Bolliger, N. P. Re, and D. C. Davis, "An Analysis of Downstream Uncertainty in NRHO Stationkeeping Strategies," AIAA/AAS Spaceflight Mechanics Meeting, San Diego, California, January 2022.

[7] Davis, D. C., E. M. Zimovan-Spreen, S. T. Scheuerle, and K. C. Howell, "Debris Avoidance and Phase Change Maneuvers in Near Rectilinear Halo Orbits," AAS Guidance, Navigation, and Control Conference, Breckenridge, California, February 2022.

[8] Lee, D.E., "Gateway Destination Orbit Model: A Continuous 15 Year NRHO Reference Trajectory," NASA Johnson Space Center White Paper, August 20, 2019.

[9] Grebow, D., M. Ozimek, K. Howell, and D. Folta, "Multi-Body Orbit Architectures for Lunar South Pole Coverage," Journal of Spacecraft and Rockets, Vol. 45, No. 2, 2008, pp. 348–358.

[10] Folta, D., M. Woodard, and D. Cosgrove, "Stationkeeping of the First Earth-Moon Libration Orbiters: The ARTEMIS Mission," AAS/AIAA Astrodynamics Specialist Conference, Girdwood, Alaska, August 2011.

[11] Petersen, J. and J. Brown, "Applying Dynamical Systems Theory to Optimize Libration Point Orbit Stationkeeping Maneuvers for WIND," AAS/AIAA Astrodynamics Specialists Conference, San Diego, California, August 2014.

[12] Muralidharan, V. and K. C. Howell, "Orbit Maintenance Strategy for Earth-Moon Halo Orbits," 31st AAS/AIAA Spaceflight Mechanics Meeting, Charlotte, North Carolina (Virtual), February 2021.

[13] Thompson, M. R., M. Bolliger, N.P. Re, and D. C. Davis, "An Analysis of Downstream Uncertainty in NRHO Stationkeeping Strategies," AIAA/AAS Astrodynamics Specialists Conference, San Diego, California, January 2022.